🔓 **Open Access**

Classical Ghost Imaging: A Comparative Study of Algorithmic Performances for Image Reconstruction in Prospect of Plenoptic Imaging

Marie Braasch
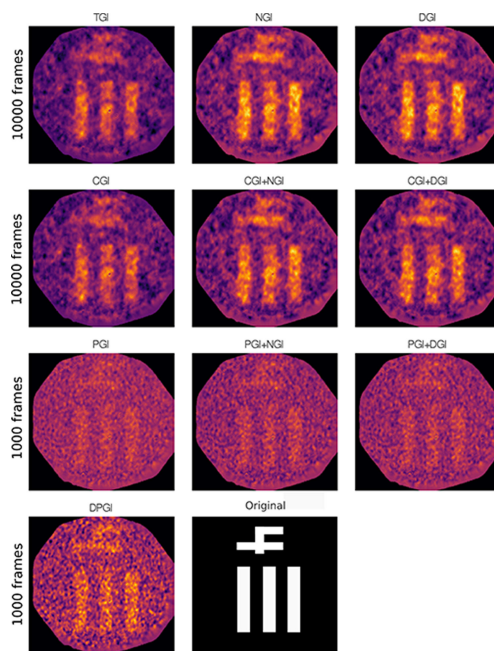**V. F. Gili**
Thomas Pertsch
Frank Setzpfandt

Classical Ghost Imaging: A Comparative Study of Algorithmic Performances for Image Reconstruction in Prospect of Plenoptic Imaging

Marie Braasch, V. F. Gili [iD], Thomas Pertsch, and Frank Setzpfandt

Institute of Applied Physics, Abbe Center of Photonics, Friedrich-Schiller-Universität Jena, Jena 07745, Germany

Abstract: Ghost Imaging has been extensively explored for 25 years for a two reasons: the rich physics of second-order photon correlations that enable this imaging scheme and the possibility of implementing new imaging protocols with interesting real-life applications, e.g. imaging in turbulent media, investigation of sensitive samples in low-flux regimes, 3-D plenoptic imaging, and so on. Since the first demonstration of Ghost Imaging, several extended versions of the Traditional Ghost Imaging algorithm have been proposed, such as Correspondence Ghost Imaging, Pseudo-Inverse Ghost Imaging, and normalization techniques that rely on different computational approaches to obtain the image from measured data. So far, a direct comparison of all above-mentioned protocols for the same experimental parameters is still lacking. In this work, we experimentally and numerically implement a number of different methods and systematically compare them in terms of the obtained SNR and computational cost. Furthermore, we investigate their compatibility with Correlation Plenoptic Imaging, a technique strictly connected to Ghost Imaging, that allows refocusing of images, increasing the depth of field (DOF) and making 3D visualization possible. Our results can provide useful guidelines for the choice of a suitable numerical algorithm for in the light of Ghost Imaging applications.

Index Terms: Classical ghost imaging, Plenoptic imaging, Image reconstruction, Speckle correlations.

1. Introduction

Ghost Imaging (GI) is a fascinating and widely studied technique exploiting spatial or momentum correlations between two beams of light. One of them interacts with the target to be imaged, where the reflected or transmitted signal is collected by a detector with a large numerical aperture but without the ability to spatially resolve the detected field, the so-called bucket detector. The other beam is instead imaged by a spatially resolving detector. Neither of the two measurements

alone contains enough information to reconstruct the image. However, computing the second order correlation function between the two measurements allows to retrieve the image [1]. GI, theoretically predicted in 1994 [2], was first demonstrated using photon correlations stemming from a spontaneous parametric down conversion (SPDC)-based entangled photon pair source [3]. A few years later, it was discovered that quantum entanglement is not a necessary condition for GI, and several independent experiments proved that classical sources, exhibiting analogous position or momentum correlations, enable GI as well [4]–[7]. Another similarly fascinating imaging technique is Plenoptic Imaging (PI) [8], [9]. By inserting a micro lens array in the image plane in front of the sensor, several sub images of the lens providing different perspectives of the scene can be formed, resulting in a larger Depth Of Field (DOF) compared to standard imaging. Each pixel encodes spatial distribution and propagation direction of the light simultaneously. This technique provides a simple and fast single-shot 3D image generation. It allows to refocus an out of-focus image in post processing without using several detectors, multiple shots or time consuming scanning techniques. Lately a new technique, namely Correlation Plenoptic Imaging (CPI) [10], [11] has been proposed, combining GI and PI. By replacing the bucket detector in Ghost Imaging by a second detector array, directional and spatial information can be acquired simultaneously, similar to PI. By appropriate pixel to pixel correlation of each frame, an out-of-focus target can be refocused in post processing, further increasing the DOF and opening up a method for applications like 3D imaging and microscopy.

Over the years years, several image reconstruction algorithms based on the standard GI correlation computation, which throughout this manuscript will be labelled as Traditional Ghost Imaging (TGI), have been proposed with the purpose of enhancing the SNR or alleviating the computational cost. Correspondence Ghost Imaging (CGI) has been claimed to yield superior results compared to TGI with a smaller number of frame accumulations and faster computation times, by computing positive and negative images through frame summations instead of multiplications [12]–[16]. More recently, Pseudo-Inverse Ghost Imaging (PGI) was introduced, in which the authors rewrite the mathematical expression to reconstruct the image in terms of a product of a matrix with its transposed. The object is reconstructed by replacing the transposed with the Moore-Penrose pseudo-inverse matrix [17]. In parallel with these three computational methods, two different normalization variants have been proposed as well. Both can be easily combined with the aforementioned protocols. Differential Ghost Imaging (DGI) has been introduced to rule out any noise coming from the source, allowing a great SNR enhancement with respect to TGI, especially in the case of samples with small average transmission function [18], [19]. A similar method, namely Normalized Ghost Imaging (NGI), was later introduced to supposedly eliminate any external sources of noise by normalizing each individual intensity value of the bucket detector rather than the average alone [20]. Finally, a couple of denoising protocols, named Denoising Pseudo-Inverse Ghost Imaging (DPGI) [21] and Iterative Pseudo-Inverse Ghost Imaging (IPGI) [22] have been demonstrated in the frame of PGI, where the computation of the Moore-Penrose pseudo-inverse can lead to stability issues [23]. Recently, Comprssive Ghost Imaging [24] and Deep-Learning Ghost Imaging [25] have been demonstrated, allowing to reduce the number of acquisitions necessary to reconstruct an image. Here however we focus our attention on methods which directly compute the two-photon correlations. In principle, all of these can be further improved and combined with Compressed Ghost Imaging and Deep Learning Ghost Imaging.

So far, a direct comparison between the computational methods under the same experimental conditions is still lacking in the literature. Hence, in this work we present a comparative study of TGI, CGI and PGI, their combination with normalization variants NGI and DGI, as well as DPGI, which is based on PGI, in terms of SNR and computational cost. Moreover, for these methods exist different protocols to normalize or denoise the image data, which improve the Signal-to-Noise Ratio (SNR). Additionally, the compatibility of these algorithms with CGI is explored. To our knowledge only the Traditional Ghost Imaging algorithm has been discussed in combination with it. In Sec. II we first review the theory of the protocols just mentioned, in Sec. III we subsequently describe the experimental setup, and follow by presenting our comparative results in terms of SNR, computational cost and compatibility with the algorithm for Correlation Plenoptic Ghost Imaging. Finally we conclude our results in Sec. IV
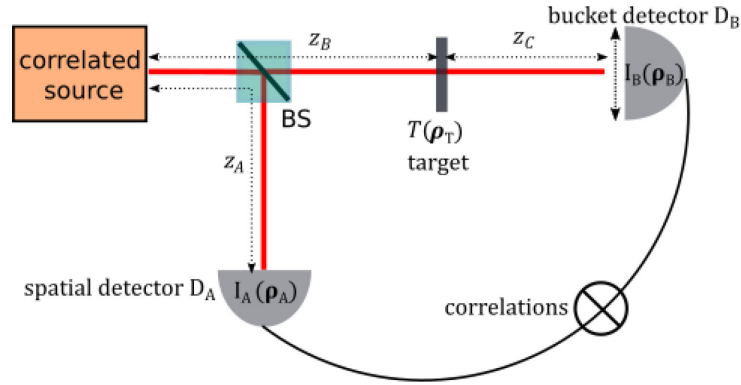
Fig. 1. Scheme of a ghost imaging experiment. A beam splitter (BS) separates the beam coming from a correlated source into two arms. A spatially resolving detector placed at distance z_A from the source measures an intensity pattern $I_A(\rho_A)$, while a bucket detector D_B placed behind a target with transmission function $T(\rho_T)$ measures intensity I_B. Evaluating the correlations between the two measurements allows to retrieve the ghost image.

2. Theory

2.1 Traditional Ghost Imaging

Let us consider the setup shown in Fig. 1. Light coming from a (pseudo-)thermal source is split into two copies by means of a 50:50 Beamsplitter (BS). A spatially resolving detector D_A placed at distance z_A from the source measures an intensity pattern $I_A(\rho_A)$ in the target-less path, while in the second path a target characterized by a transmission function $T(\rho_T)$ is placed at distance z_B from the source, $\rho_{A,B,T}$ represent the coordinates on the respective detector-, target plane. A bucket detector placed behind the target at distance z_C measures intensities I_B [26]. Depending on the distances z_A, z_B, z_C it is possible to achieve ghost imaging if $z_A = z_B$ or ghost diffraction if $z_A = z_B + z_C$ [27].

The classical statistical correlation of the intensity fluctuations can be expressed as [28]:

$$\langle\, I_A(\rho_A) I_B(\rho_B)\rangle = \langle I_A(\rho_A)\rangle\langle I_B(\rho_B)\rangle + \langle\Delta I_A(\rho_A)\Delta I_B(\rho_B)\rangle, \tag{1}$$

where $\langle I_A(\rho_A)\rangle$ and $\langle I_B(\rho_B)\rangle$ are the mean Intensities measured by detector D_A or D_B respectively. The second term represents the intensity fluctuation correlation. The notation $\langle\ldots\rangle$ represents the ensemble average. By inserting $\Delta I_i(\rho_i) = I_i(\rho_i) - \langle I_i(\rho_i)\rangle$, in the second term, the ghost image can be computed by means of the following equation [26]:

$$T(\rho_A) = \left\langle \int d\rho_B^2 \Delta I_A(\rho_A)\Delta I_B(\rho_B)\right\rangle. \tag{2}$$

In the discrete case, defined by the finite frame rate and pixel size of a real spatially resolving detector 2 reduces to:

$$\mathbf{T}_{\text{TGI}} = \sum_{n=1}^{N} \left(\mathbf{A}_n - \langle\mathbf{A}\rangle\right)\left(B_n - \langle B\rangle\right), \tag{3}$$

respectively. N represents the number of frames acquired during the experiment. If $\mathbf{A}_n, \mathbf{B}_n$ are bold we are talking about a spatially resolved Image, hence bold $\mathbf{A}_n, \mathbf{B}_n$ are a matrix containing the intensity values of the n'th frame. If they are not bold, A_n, B_n represent the average over the whole detector array (or the value a bucket detector would measure).

2.2 Correlation Plenoptic Imaging

As mentioned in the introduction, CPI is an extension of Ghost Imaging. A theoretical proof of concept was provided by [29] for entangled photons and by [30] for classical light.
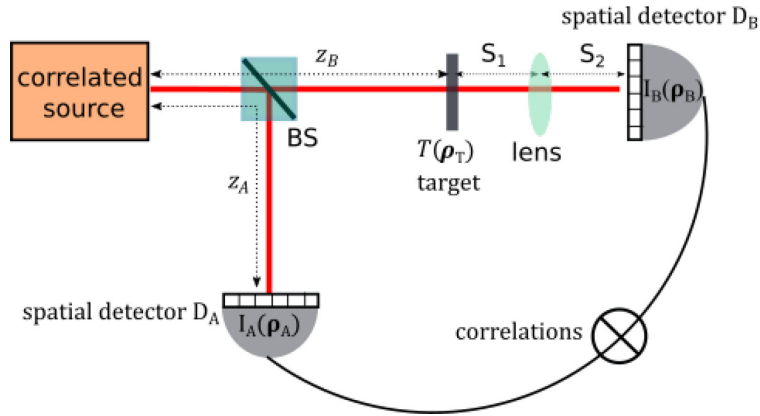
Fig. 2. A possible imaging scheme for CPI with classical light. The source is focused by the lens on detector D_B, the Ghost Image is constructed by correlation with detector D_A.

The general idea is as follows: by replacing the bucket detector by an imaging array, the spatial and directional information of the light field can be acquired simultaneously, allowing us to refocus out-of-focus data and enabling us to perform 3D-Imaging, similarly to standard PI (please refer to [8], [9] for more details). Since we are using two detectors, the image formation and the acquisition of directional information get decoupled. Therefore, resolution and DOF are only limited by the fundamental limits of wave optics and the detector resolution. This way, the drawback of standard PI, namely the trade-off between resolution and DOF, is overcome. A disadvantage in comparison to standard PI is, that in Ghost Imaging schemes, several frames have to be acquired. This means the advantage of single shot acquisition is lost. One possible solution to the problem was proposed by Ref. [31], where the authors use a source with a wide spectral range in combination with a spectrometer to acquire multiple images at once. Different setups to realize the scheme have been compared in [32], one of them is depicted in Fig. 2. The setup requires meticulous alignment to guarantee the pixel correlations are preserved. In the depicted setup the condition

$$f_1 = \frac{1}{S_2} + \frac{1}{z_B + S_1} \tag{4}$$

must be fulfilled in order to satisfy the thin lens equation and image the source on detector D_B, thus directly imaging directional information. If $z_A = z_B$ the target is in focus and Detector D_A images the speckle field in the object plane. Any plane for which the focusing condition is not fulfilled can be refocused in post processing using the following, refocusing equation [10], [32]:

$$T_{ref}(\boldsymbol{\rho}_A) = \left\langle \int d^2\boldsymbol{\rho}_B \Delta I_A(\alpha \boldsymbol{\rho}_A + \beta \boldsymbol{\rho}_B) \Delta I_B(\boldsymbol{\rho}_B) \right\rangle, \tag{5}$$

$$(\alpha, \beta) = \left(\frac{z_A}{z_B}, M\left(1 - \frac{z_A}{z_B}\right) \right), \tag{6}$$

with magnification $M = S_2/(S_1 + z_B)$, α and β are the rescaling and shifting factors depending on the distances within the setup. In the focused case $z_A = z_B$ ($\alpha = 1$, $\beta = 0$), the equation 5 reduces to TGI, eq. 2. Looking at eq. 5 and eq.6, we can see that the refocusing process is a simple rescaling and shifting of the pixels at detector D_A with the factors depending on the distance between the in- and out-of-focus plane. In the discrete case, the adjusted equation reduces to:

$$T_{TGI}[i, j] = \sum_n^N \sum_{p_{min}}^{p_{max}} \sum_{q_{min}}^{q_{max}} \left(\mathbf{A}_n[i'(p, q), j'(p, q)] - \langle \hat{\mathbf{A}}[i'(p, q), j'(p, q)] \rangle \right)$$

$$- \left(\mathbf{B}_n[p, q] - \langle \hat{\mathbf{B}}[p, q] \rangle \right), \tag{7}$$

with p_{min}, q_{min} and p_{max}, q_{max} defined such that $i,' j' \geq 1$ and $i,' j' \leq N$, respectively; i', j' are in turn introduced by:

$$i' = g^{-1}(f(g(i), g(p), \alpha, \beta)), \tag{8}$$

$$j' = g^{-1}(f(g(j), g(q), \alpha, \beta)), \tag{9}$$

$$f(i, p, \alpha, \beta) = \alpha i + \beta p. \tag{10}$$

The values in square brackets refer to the integer pixel indices, function f is the function shifting and rescaling the frame according to eq. 6. The function $g(x) = x - (l + 1)/2$ translates the pixel indices into a coordinate system which is centered at 0, such that negative values are allowed and the shift is scaled correctly, since the refocusing equation assumes radial coordinates. At the end we have to transform back to integer pixel values which is achieved by applying $g^{-1}(x) = x + (l + 1)/2$.

2.3 Differential and Normalized Ghost Imaging

In DGI, the bucket detector contribution to the ghost image is reweighed with a reference signal. This method employs the integrated signal measured by the spatially resolving detector to do so [18], [19]:

$$(B_n - \langle B \rangle) \rightarrow \left(B_n - A_n \frac{\langle B \rangle}{\langle A \rangle} \right), \tag{11}$$

where the sum is performed over pixel indexes of the spatially resolving detector i, j, and the total pixel number is $I \cdot J$. By normalizing with a reference signal, noise sources such as power fluctuations in the source can be eliminated or diminished. Furthermore, it can be shown that the ratio of the SNR between DGI and TGI reads [18]

$$\text{SNR}_{\text{DGI}}/\text{SNR}_{\text{TGI}} = 1 + \left((\overline{T})^2 / \overline{\delta T^2} \right), \tag{12}$$

with $\overline{T}$ the average and $\overline{\delta T^2}$ the variance of the transmission function. Thus, the DGI protocol allows for great SNR improvements for highly transparent samples, paving the way towards GI investigation of non-binary targets, such as biological samples. In NGI, each individual intensity value of the bucket detector is normalized instead of the average signal. Thus, this method allows eliminating also external sources of noise other than the source itself [20]. This protocol can be computed as follows:

$$(B_n - \langle B \rangle) \rightarrow \left(\frac{B_n}{A_n} - \frac{\langle B \rangle}{\langle A \rangle} \right). \tag{13}$$

This protocol was shown to theoretically perform exactly in the same way as DGI in terms of SNR [20], with possible differences in numerical values being due to the two algorithms rounding real numbers at different stages of the correlation computation.

2.4 Correspondence Ghost Imaging and Its Normalized Versions

The main goal in CGI is to greatly reduce the computational cost by only using +1 or -1 weights, hence performing only matrix additions and removing the multiplication with a real number, as compared to TGI [12]. Classical ghost imaging based on thermal and pseudo-thermal sources relies on the assumption that the total intensities measured by detectors D_A and D_B are randomly varying in time and no temporal correlations are present. Thus, the deviation from the mean calculated at a certain time follows a normal distribution [12]–[14]. Therefore, we can assign positive or negative time stamps to frames for which the value measured by the bucket detector is greater or lower than the mean:

$$t_+ = \{t_n | B_n - \langle B \rangle > 0\}, \tag{14}$$

$$t_- = \{t_n | B_n - \langle B \rangle < 0\}. \tag{15}$$

As in GI the two detectors are synchronized in time, we can assume that the intensity distribution of the pixels measured by the spatially resolving detector D_A fluctuates in harmony with the bucket detector signal. Hence, the frames collected by can be divided into subsets according to the sign of :

$$(B_n - \langle B \rangle) : \left\{ A_n^+ | B_n - \langle B \rangle > 0 \right\},$$

$$\left\{ A_n^- | B_n - \langle B \rangle < 0 \right\}. \tag{16}$$

Once the subsets are defined, positive and negative ghost images can be generated by taking the arithmetic average over $\{A_n^+\}$ and $\{A_n^-\}$, respectively [12]. In an alternative definition of CGI [13], further subsets can be created by also comparing the total intensity measured by the imaging detector to its mean value:

$$A_n^{++} | B_n - \langle B \rangle > 0, \; A_n - \langle A \rangle > 0, \tag{17}$$

$$A_n^{+-} | B_n - \langle B \rangle > 0, \; A_n - \langle A \rangle < 0, \tag{18}$$

$$A_n^{-+} | B_n - \langle B \rangle < 0, \; A_n - \langle A \rangle > 0, \tag{19}$$

$$A_n^{--} | B_n - \langle B \rangle < 0, \; A_n - \langle A \rangle < 0. \tag{20}$$

By averaging over each subset we end up with four images R^{++}, R^{+-}, R^{-+}, R^{--}. Finally, the ghost image can be retrieved by:

$$\mathbf{T}_{\text{CGI}} = \mathbf{R}^{++} + \mathbf{R}^{+-} - \mathbf{R}^{-+} - \mathbf{R}^{--}. \tag{21}$$

This second method of implementing CGI has been shown to yield increased SNR performances with respect to the previous one [13]. In our comparative analysis we focused our attention on this second implementation. Compared to TGI, it was claimed that in CGI the number of necessary frame acquisitions can greatly reduce, since only the ones for which the intensity measured by the bucket detector is far from the mean consistently contribute to the SNR. However, identifying such frames among the data set can be a computationally more expensive task than just using them. It is important to stress that while second-order correlations of the joint intensity distribution are not directly evaluated in this protocol, we can interpret the quantities R^{++}, R^{+-}, R^{-+}, R^{--} as averages over a conditional sampling distribution, which is still related to the joint distribution through Bayes' theorem. A combination of NGI and DGI with CGI has been proven to be rather straightforward, confirming the noise-reduction capabilities of normalization variants [15], [16]. It should be noted that in CGI, contrarily to TGI, a combination with NGI and DGI methods yields exactly identical results, both theoretically and numerically, because the normalization choice does not affect the sorting mechanism of CGI. This is fully confirmed by our calculations. The normalized variants can be computed by evaluating subsets:

$$A_n^{++} | S(B_n) - \langle S(B) \rangle > 0, \; A_n - \langle A \rangle > 0, \tag{22}$$

$$A_n^{+-} | S(B_n) - \langle S(B) \rangle > 0, \; A_n - \langle A \rangle < 0, \tag{23}$$

$$A_n^{-+} | S(B_n) - \langle S(B) \rangle < 0, \; A_n - \langle A \rangle > 0, \tag{24}$$

$$A_n^{--} | S(B_n) - \langle S(B) \rangle < 0, \; A_n - \langle A \rangle < 0. \tag{25}$$

With

$$S(B_n) = B_n - \frac{\langle B \rangle}{\langle A \rangle} A_n, \tag{26}$$

for CGI+DGI and

$$S(B_n) = \frac{B_n}{A_n} - \frac{\langle B \rangle}{\langle A \rangle}, \tag{27}$$

for CGI+NGI. The ghost image is then generated analogously.

2.5 Pseudo-Inverse Ghost Imaging

In order to define PGI, it is convenient to rewrite TGI into a more compact matrix form [17], [21]:

$$\mathbf{T}_{\text{TGI}} = \frac{1}{N} (\boldsymbol{\Phi} - \mathbf{I}\langle\boldsymbol{\Phi}\rangle)^T (\boldsymbol{B} - \mathbf{I}\langle\boldsymbol{B}\rangle),
\tag{28}$$

where $\boldsymbol{B}$ and $\boldsymbol{I}$ are $(N \times 1)$-column vectors, $\boldsymbol{I}$'s elements are all equal to 1, $\boldsymbol{B}$ contains the N bucket detector values, with $\langle\boldsymbol{B}\rangle$ being their average, $\boldsymbol{\Phi}$ is a $(N \times (IJ))$-matrix whose rows represent each image measured by the detector, and finally $\langle\boldsymbol{\Phi}\rangle$ is a $(1 \times (IJ))$-row vector containing the mean values over all acquired frames for each pixel. Since the components of $\boldsymbol{B}$ are related to the transmission function of the object by $B_n = \int A_n(x, y)T(x, y)\,dx\,dy$, TGI can be rewritten in an even more compact form:

$$\mathbf{T}_{\text{TGI}} = \frac{1}{N} \boldsymbol{\Psi}^T \boldsymbol{\Psi} \mathbf{T},
\tag{29}$$

where $\boldsymbol{\Psi} = \boldsymbol{\Phi} - \mathbf{I}\langle\boldsymbol{\Phi}\rangle$, and $\boldsymbol{T}$ is a $((IJ)) \times 1$-column vector containing the transmission function of the object. In this compact formula it is evident that in the noise-less ideal case $\boldsymbol{\Psi}^T \boldsymbol{\Psi} = \text{Id}$, and $\mathbf{T}_{\text{TGI}}$ is a perfect representation of the transmission function. In PGI $\boldsymbol{\Psi}^T$ is substituted with the Moore-Penrose pseudo-inverse matrix $\boldsymbol{\Psi}^\dagger$, a generalization of the inverse for non-square matrices [34]. This method has been claimed to yield better SNR performances than TGI and even DGI [17]. The Normalized and Differential versions of PGI can be subsequently introduced by performing the equation modifications explained in the sections above. The main issue with this protocol, however, is that the computational stability of the Moore-Penrose pseudo-inverse often depends on the employed algorithm [23]. The main source of this noise is the appearance of non-correlated off-diagonal elements in the scalar matrix $\boldsymbol{\Psi}^\dagger \boldsymbol{\Psi}$. The off-diagonal noise can be reduced by introducing Denoising (DPGI) and Iterative Pseudo-Inverse Ghost Imaging (IPGI) [21]. These algorithms build upon each other and allow to eliminate any off-diagonal entries in $\boldsymbol{\Psi}^\dagger \boldsymbol{\Psi}$ that are smaller than a certain threshold. The idea is to split the product under question into a diagonal matrix $\boldsymbol{s} = \text{diag}(\boldsymbol{\Psi}^\dagger \boldsymbol{\Psi})$, and a noise matrix $\boldsymbol{n} = \boldsymbol{\Psi}^\dagger \boldsymbol{\Psi} - \text{diag}(\boldsymbol{\Psi}^\dagger \boldsymbol{\Psi})$. Then:

$$\mathbf{T}_{\text{PGI}} = \frac{1}{N} \boldsymbol{\Psi}^\dagger \boldsymbol{\Psi} \mathbf{T} = \frac{1}{N}(\boldsymbol{s} + \boldsymbol{n})\mathbf{T}.
\tag{30}$$

In DPGI the result of the PGI algorithm is used as an initial value with the goal of approximating the actual noise coming from the physical system and discarding the one coming from the algorithm, using a threshold t:

$$\mathbf{T}_{\text{DPGI}} = \frac{1}{N}(\boldsymbol{s} + \boldsymbol{n})\mathbf{T} - \frac{1}{N}n''\mathbf{T}_{\text{PGI}},
\tag{31}$$

$$n' = \begin{cases} n[i, j], & n[i, j] > t \\ 0, & n[i, j] < t. \end{cases}
\tag{32}$$

Finally, in IPGI the noise coming from off-diagonal elements is reduced even further with the following iteration:

$$\mathbf{T}_{\text{IPGI}}^{(k+1)} = \mathbf{T}_{\text{PGI}} - \frac{1}{N}n'\mathbf{T}_{\text{IPGI}}^{(k)},
\tag{33}$$

where the initial conditions are $\mathbf{T}_{\text{IPGI}}^{(0)} = \mathbf{T}_{\text{PGI}}$, $\mathbf{T}_{\text{IPGI}}^{(1)} = \mathbf{T}_{\text{DPGI}}$.

3. Experiment and Discussion

3.1 Setup

In this section, we present our results comparing TGI, CGI, PGI and their normalized versions. The used experimental setup is analogous to the one depicted in Fig. 1. Our pseudo-thermal light source consists of a CW laser operating at $\lambda = 450$ nm, with an output power of 50 mW, impinging
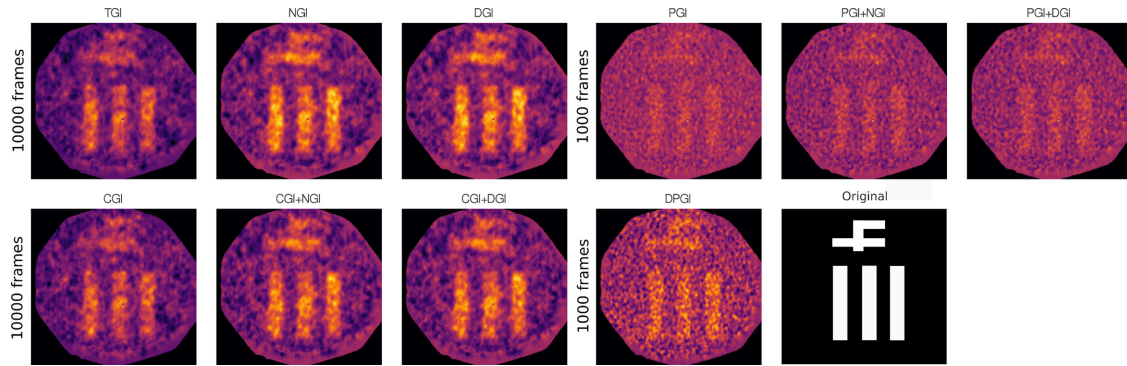
Fig. 3. Visual comparison of Ghost Images of a standard USAF test target. TGI, CGI and their normalization variants are evaluated with 10 000 frames. PGI, its normalization variants and DPGI were only calculated with 1000 frames due to RAM limitations.

on a rotating ground glass plate with 220 grit, at $r = 10$ mm from the rotational axis, and with a beam radius of 1.5 mm, effectively breaking the spatial coherence of the laser beam and creating a speckle pattern. The rotational speed was kept in the range $0.5°/s − 2°/s$, resulting in source coherence times of 2.5 s–30.5 s. The generated speckle pattern is separated into two correlated beams by means of a 50:50 beam splitter, the object and reference beams. In the object path we place an USAF test target (Thorlabs R3L3S1N) at the same distance from the source (imaging configuration) as a CMOS silicon camera (Thorlabs DCC1545 M) performing the spatially resolved detection in the reference path. Light transmitted by the sample is focused on a second identical CMOS camera, whose pixel-wise measured intensities are summed to effectively generate a bucket detector signal. We made the choice to simulate a bucket detector signal with a second identical camera to easily interchange between GI and CPI configurations. According to the quantum efficiency and noise characteristics of the employed detector, as well as the operation regime, whether quantum or classical, single photodiodes can yield better bucket detector performances in the case of classical GI, while other technologies such as ICCD or sCMOS are more suitable in the quantum regime [33]. Since in our experimental implementation we employ two CMOS cameras, the bucket detector term in the GI formula, $B_i − \langle B \rangle$, is evaluated as:

$$(B_i − \langle B \rangle) = \frac{1}{IJ} \sum_{I,J}^{i,j} (B_n[i, j] − \langle B[i, j] \rangle), \qquad (34)$$

such that B_n is a number resulting from the sum over the pixel values $B_n[i, j]$ of the n'th frame, normalized with the total pixel number $I \cdot J$. Correlation calculations and further data analysis are performed with Julia v1.3 on a 64-bit, 32 GB RAM desktop computer with an AMD Ryzen 5 1600 Six-Core processor at 3.6 GHz. Fig. 3 allows for a visual comparison of the different ghost images we obtain. For PGI-based algorithms we place an upper limit of 1000 frames in our analysis due to RAM limitations.

3.2 Signal-to-Noise Ratio (SNR) Analysis

In order to quantitatively compare the methods mentioned so far, we evaluate the SNR with the following expression:

$$\text{SNR}_{GI} = 10 \log_{10} \left[\frac{IJ}{\sum_{i,j} (T[i, j] − T_{GI}[i, j])^2} \right]. \qquad (35)$$

Here, $T[i, j]$ is the reference image and I, J are the total number of pixels along the x and y axes, respectively. This choice of the SNR expression suits our binary target case and is suitable to
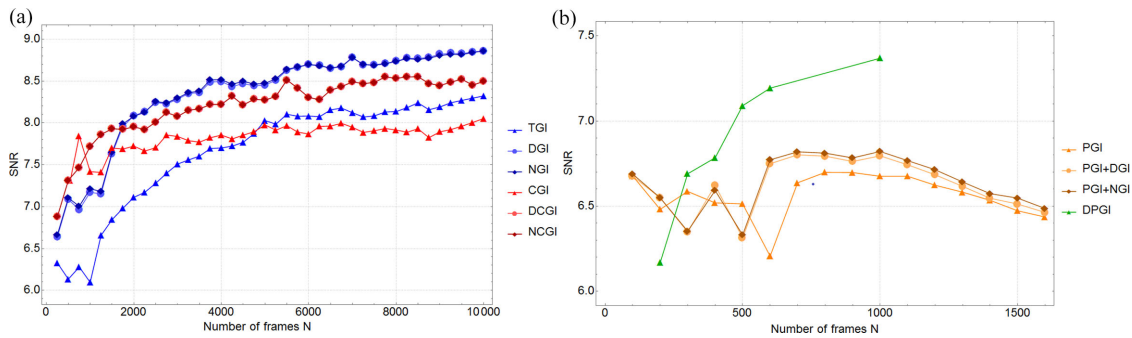
Fig. 4. Summary of the SNR behavior as a function of the number of collected frames, in the case of a) TGI, CGI and their normalized variants, and b) for PGI and related algorithms. The color code is organized so that different base algorithms are associated to different colors, blue for TGI, DGI, NGI, red for CGI, CGI+DGI, CGI+NGI, orange for PGI, PGI+DGI, PGI+NGI, green for DPGI. Different normalizations are associated to different symbols: triangles for no normalization, crosses for differential algorithms, diamonds for normalized algorithms. Note that CGI+NGI and CGI+DGI curves yield the exact same results, as anticipated in section II.

compare images of different sizes [35] The results are shown in Fig. 4, where the SNR for TGI, CGI and related normalizations are computed up to 10 000 frames, while the computational cost forced us to limit our analysis to 1600 frames for PGI-based methods, and to 1000 frames for DPGI. Overall, all normalization variants perform better than their regular versions, and no relevant difference between the two types of normalization can be noticed. This has been theoretically analyzed in [18], where the authors show that NGI and DGI would always outperform TGI, and dependending on the object size the improvement can be bigger or smaller. Therefore there is no reason not to use the normalization variants, especially in view of the fact that they can easily be combined with any other algorithm. Fig. 4 a shows that TGI outperforms CGI, and their normalized variants behave accordingly. In general, all those protocols exhibit a reasonable increase in SNR with the number of frames. Contrarily, Fig. 4 b shows that the SNRs of PGI and its normalized variants, in which the pseudo-inverse has been computed with the singular value decomposition method [17], do not steadily increase with the number of frames. We attribute this to the stability issues of the pseudo-inverse computation, with the appearance of non-zero off-diagonal elements. These cause the introduction of more and more noise terms in the computation that eventually cause a SNR decrease as the number of frames increases. The denoising algorithm DPGI fixed this issue observed for PGI, with an SNR that now increases with the number of acquired frames, as expected, and at 1000 frames exhibits a SNR similar in magnitude to that of the algorithms in Fig. 4 a. A different approach to the singular value decomposition might solve the stability issue of PGI, confirming what has been observed in the literature [21]. Theoretical analysis reported in several papers (e. g. [36], [37]) predicts that the SNR proportionally increases with the square root of the number of frames. To check whether this applies to our results, we fitted the SNR curves with a function of the type $f(x) = Ax^{0.5} + B$ (see the exemplary fit in Fig. 5). Overall, all curves follow the expected theoretical behavior, whilst the slight deviations can be explained by overlapping and repeating speckle fields after one revolution of the ground glass.

3.3 Computational Cost Analysis

In this section, we compare the computational cost of the GI-based methods. While the total computation time is dependent on the hardware used, and newer CPUs like AMD Ryzen 5 3600 could be much more efficient than our AMD Ryzen 5 1600, the general relations and trends between algorithms are generally independent of hardware, but could depend on the software used. This could explain why the claims of computational advantage of CGI and PGI over TGI were not verified in our experimental dataset. Fig. 6 shows the computation time as a function of the
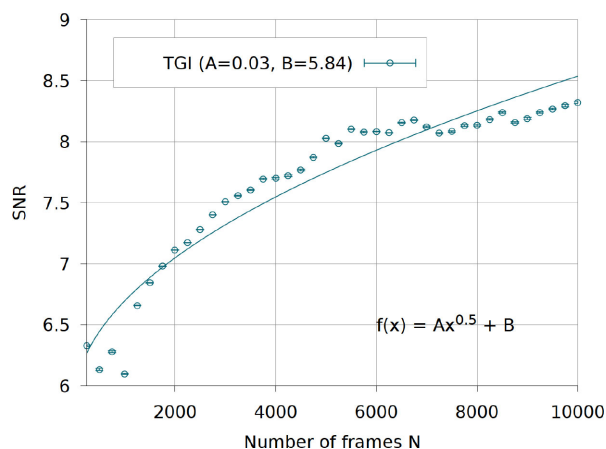
Fig. 5. Exemplary fit of the TGI measured SNR with a square root function. The two curves show a reasonable agreement, as predicted by theory [36], [37].
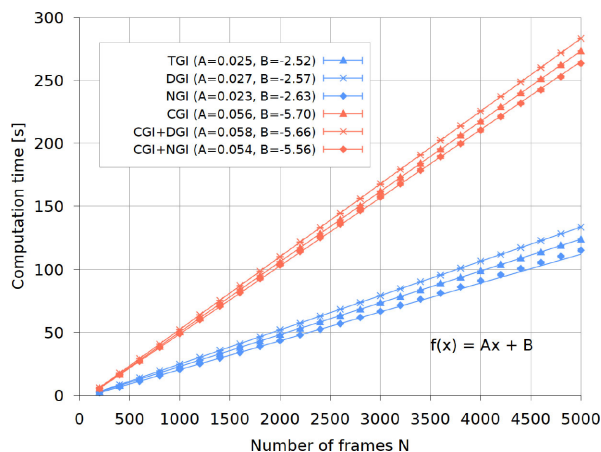

Fig. 6. Computation time as a function of the number of frames for TGI, CGI, and related normalized variants (dots), plotted together with linear fit functions (solid lines).

number of frames for TGI, CGI, and related normalizations, together with their linear fit functions. In order to have comparable results the image dimension was kept constant at 800×800 pixels.

The first noticeable point is, that the normalization does not significantly affect the computational cost. Secondly, as opposed to the claims of [12], for our implementation CGI and its normalizations run slower than TGI and its normalizations. In particular, the CGI-based algorithms run at a rate of 54.11 ms/frame-57.79 ms/frame, whereas than TGI, NGI and DGI need 22.90 ms/frame-27.22 ms/frame. This could be attributed to the greater efficiency of Julia in matrix multiplications with real numbers, compared to conditional statement evaluation, which is the basis for CGI-based algorithms. Fig. 6 shows the computation time for PGI (Fig. 7 a) and DPGI (Fig. 7 b). Normalized variants of PGI have been omitted, as their influence on the computation time is negligible. IPGI has been omitted as well, as it is essentially a k-fold repetition of DPGI, hence its computation time will trivially be k-times the one of DPGI. A linear fit for the PGI curve reveals a rate of 172.1 ms/frames, which is almost one order of magnitude slower than TGI. DPGI instead, is significantly slower, with a rate of 83.5 s/frames. This difference is caused by the requirement of PGI and DPGI to construct, multiply and compute the pseudo-inverse of larger matrices. Such effect is illustrated in Fig. 8, where calculations were performed on a sample of 200 frames by varying the image area under analysis. While TGI, CGI and related normalizations did not exhibit a direct dependence on
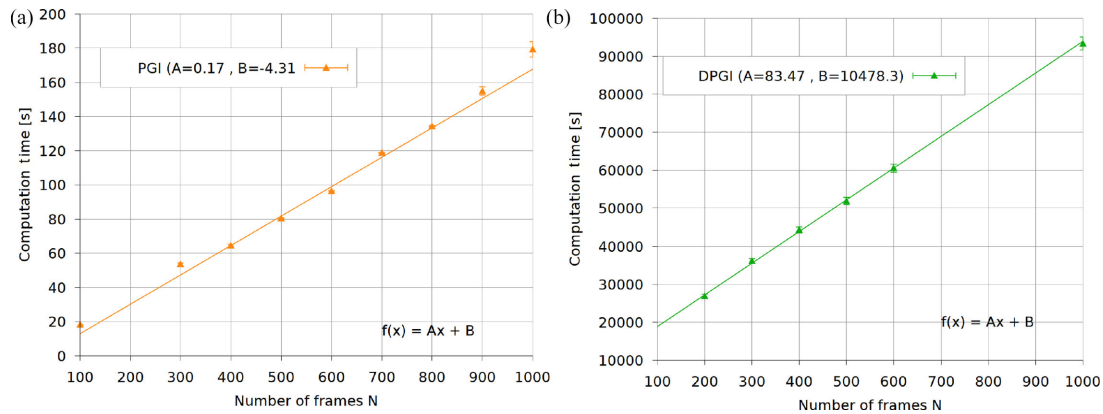
Fig. 7. Computation time as a function of the number of frames for a) PGI and b) DPGI (dots), plotted together with linear fits (solid lines).
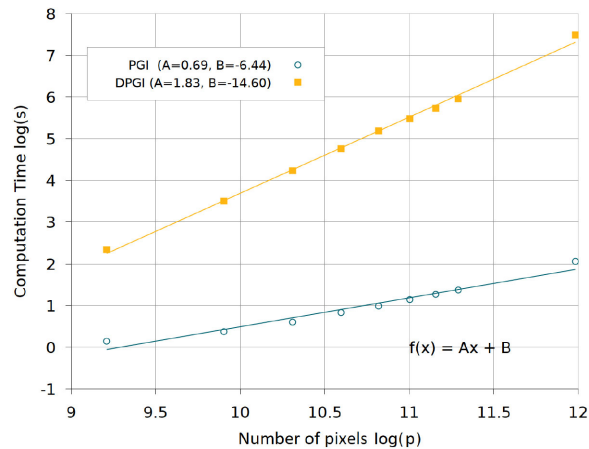

Fig. 8. Log-log plot of the computation time in PGI and DPGI as a function of the number of pixels making up the image.

the image size in the range we considered, the log-log plots for PGI and DPGI reveal a scaling of $p^{0.690}$ and $p^{1.83}$, respectively, where p is the number of pixels. These results show that DPGI runs relatively slowly for large ghost images, but could be a reasonable choice for the investigations of small image sections (e.g. 64×64). As a final remark, the application of CGI and PGI algorithms to quantum GI is not trivial, since in this case correlations between bucket and spatially resolving detectors are usually evaluated by the coincidence electronics. However, recently DGI has been successfully implemented in a quantum GI microscopy experiment [19].

3.4 Compatibility With Correlation Plenoptic Imaging

Here we want to discuss which of the investigated algorithms could be used for image reconstruction in CPI. As mentioned in Sec. II-B, we can refocus onto different imaging planes in post processing using eq.5, which rescales and shifts pixels at detector A depending on the distance between focused and out of focus plane. This means that each pixel in the resulting image is the sum of products of shifted pixels at D_A and non-shifted pixels at D_B. A generalization of CGI to construct images for CPI has been attempted by building conditional sets on detector D_A based on individual pixel values with measured by D_B, however the results proved to be inconclusive. All other algorithms can be used for image reconstruction in CPI. However, by introducing the
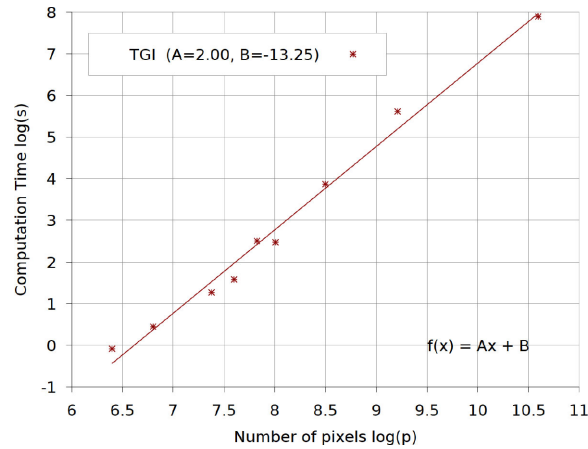
Fig. 9. Dependence of Computation time from the total number of pixels for Traditional Ghost Imaging refocusing an image for 200 frames.

TABLE I
Computation Time of Ghost Imaging Algorithms

Name	Computation Time
TGI	$\propto N$
CGI	$\propto N$
PGI	$\propto Np^{0.69}$
DPGI	$\propto Np^{1.82}$
IPGI	$\propto kNp^{1.83}$

N: Number of Frames, p: Number of pixels, k: Number of iterations.

TABLE II
Compatibility Abilities With Refocusing

Name	Ref.	Norm.	Ref.	Drawbacks
TGI	✓	DGI	✓	none
		NGI	✓	
CGI	(✗)	DGI	(✗)	no refocusing
		NGI	(✗)	so far
PGI	✓	DGI	✓	RAM intensive
		NGI	✓	unstable, slow
DPGI	✓	DGI	✓	RAM intensive
		NGI	✓	unstable, extremely slow
IPGI	✓	DGI	✓	RAM intensive
		NGI	✓	unstable, extremely slow

Overview of all implemented algorithms their drawbacks and if they and their normalization variants (Norm.) are compatible with the refocusing algorithm (Ref.).

additional summation the computation time increases drastically. Fig. 9 shows an explanatory fit of the computation time with TGI over the number of pixels, from which it can be inferred that the computation time increases by a factor of p^2. This is true for CPI with TGI, NGI and DGI as they all rely on the same pixel shifting function. Especially computationally expensive becomes image reconstruction with CPI in combination with PGI, since this method relies on matrix inversion. While for focused GI only one inversion is necessary, in CPI as many inversions as the total pixel number are needed, making its combination with PGI practically unfeasible.

4. Conclusion

In this work, we have given an overview and a quantitative comparison among several Ghost Imaging-based image reconstruction algorithms, in terms of SNR and computational cost. When analyzing SNR performances, we found that normalized and differential protocols related to Traditional Ghost Imaging (TGI) perform the best, with comparable computation times. Correspondence Ghost Imaging (CGI) and its related normalizations, contrarily to what has been stated in the literature, performed slightly worse in terms of SNR and took about twice the time of TGI and its normalizations. The computation of Pseudo-Inverse Ghost Imaging and its normalized variants was revealed to be unstable, with the SNR not increasing with the square root of number of frames as expected. The implementation of a denoising algorithm showed its potential to solve this issue and achieve similar SNR performances to those of TGI, at the cost of a much greater computation time. The latter, however, was revealed to depend strongly on the target size, making this method more suitable for imaging of small objects. Overall, Differential and Normalized Ghost Imaging variants are the most promising algorithms in the light of applications, as they allow for high-SNR imaging of non-binary and low transmissive targets. Furthermore, in many cases other methods can be used in conjunction with these normalization variants.

An overview of the results regarding the computation time is in Table I. Furthermore we found, that any technique can be used for image reconstruction in Correlation Plenoptic Imaging, with the exception of CGI, for which no meaningful generalization has been found yet. Also, by introducing the sum in the evaluation for each pixel the computation time increases drastically. In the case of PGI the computation becomes especially expensive as we need as many image inversions as pixels per image for each image ($I \cdot J \cdot N$ inversion evaluations), making this method too computationally expensive to be of practical use. All things considered DGI or NGI would be the best choices in between the algorithms under consideration for image reconstruction in CPI. An overview of the results as well as the strengths and weaknesses of each algorithm are presented in Table II.

Our results aim at better understanding and compare the wide number of results and approaches present in the literature on ghost imaging, with the goal of providing a few guidelines for real-life imaging applications of Ghost Imaging and Correlation Plenoptic Imaging.

References

[1] J. H. Shapiro and R. W. Boyd, "The physics of ghost imaging," *Quantum Inf. Process. ed.*, vol. 11, pp. 949–993, Jan. 2012, doi: 10.1007/s11128-011-0356-5.

[2] A. V. Belinskii and D. N. Klyshko, "Two-photon optics: Diffraction, holography, and transformation of two-dimensional signals," *J. Exp. Theor. Phys.*, vol. 105, pp. 487–493, Mar. 1994.

[3] T. B. Pittman, Y. H. Shih, D. V. Strekalov, and A. V. Sergienko, "Optical imaging by means of two-photon quantum entanglement," *Phys. Rev. A*, vol. 52, no. 5, pp. R3429–R3430, Nov. 1995, doi: 10.1103/PhysRevA.52.R3429.

[4] R. S. Bennink, S. J. Bentley, and R. W. Boyd, "'Two-photon' coincidence imaging with a classical source," *Phys. Rev. Lett.*, vol. 89, no. 11, Aug. 2002, Art. no. 113601(4), doi: 10.1103/PhysRevLett.89.113601.

[5] A. Gatti, E. Brambilla, M. Bache, and L. A. Lugiato, "Ghost imaging with thermal light: Comparing entanglement and classical correlation," *Phys. Rev. Lett.*, vol. 93, no. 9, Aug. 2004, Art. no. 093602(4), doi: 10.1103/PhysRevLett.93.093602.

[6] A. Valencia, G. Scarcelli, M. D´Angelo, and Y. Shih, "Two-photon imaging with thermal light," *Phys. Rev. Lett.*, vol. 94, Feb. 2005, Art. no. 036301(4), doi: 10.1103/PhysRevLett.94.063601.

[7] D. Zhang, X. H. Chen, Y. H. Zhai, and L. A. Wu, "Correlated two-photon imaging with true thermal light," *Opt. Lett.*, vol. 30, no. 18, pp. 2354–2356, Sep. 2005, doi: 10.1364/OL.30.002354.

[8] E. H. Adelson and J. Y. Wang, "Single lens stereo with a plenoptic camera," *IEEE Trans. Pattern Anal. Mach. Intell.*, vol. 14, no. 2, pp. 99–106, Feb. 1992, doi: 10.1109/34.121783.

[9] R. Ng, M. Levoy, M. Brédif, G. Duval, M. Horowitz, and P. Hanrahan, "Light field photography with a handheld plenoptic camera," Comput. Sci. Tech. Rep. CSTR 2005-02, Jan. 2005.

[10] M. D'Angelo, F. V. Pepe, A. Garuccio, and G. Scarcell, "Correlation plenoptic imaging," *Phys. Rev. Lett.*, vol. 116, Jun. 2016, Art. no. 223602, doi: 10.1103/PhysRevLett.116.223602.

[11] M. D'Angelo, F. V. Pepe, A. Garuccio, and G. Scarcelli, "Correlation plenoptic imaging: An overview," *Appl. Sci.* vol. 8, no. 10, 1958, Oct. 2018, doi: 10.3390/app8101958.

[12] K. H. Luo, B. Q. Huang, W. M. Zheng, and L. A. Wu, "Nonlocal imaging by conditional averaging of random reference measurements," *Chin. Phys. Lett.*, vol. 29, no. 7, Jun. 2012, Art. no. 0742016(5), doi: 10.1088/0256-307X/29/7/074216.

[13] S. C. Song, M. J. Sun, and L. A. Wu, "Improving the signal-to-noise ratio of thermal ghost imaging based on positive-negative intensity correlations," *Opt. Commun.*, vol. 366, pp. 8–12, May 2016, doi: 10.1016/j.optcom.2015.12.045.

[14] X. Yao, X. Liu, W. Yu, and G. Zhai, "Correspondence imaging based on correlation coefficients," *Chin. Opt. Lett.*, vol. 13, no. 1, Jan. 2015, Art. no. 010301, doi: 10.3788/COL201513.010301.

[15] M. F. Li, Y. R. Zhang, K. H. Luo, L. A. Wu, and H. Fan, "Time-correspondence differential ghost imaging," *Phys. Rev. A.*, vol. 87, Mar. 2013, Art. no. 033813(5), doi: 10.1103/PhysRevA.87.033813.

[16] G. Li *et al.*, "Iterative normalized correspondence ghost imaging," *Optik*, vol. 161, pp. 20–26, May 2018, doi: 10.1016/j.ijleo.2018.02.005.

[17] C. Zhang, S. Guo, J. Cao, J. Guan, and F. Gao, "Object reconstitution using pseudo-inverse for ghost imaging," *Opt. Exp.*, vol. 22, no. 24, pp. 30063–30073, Nov. 2014, doi: 10.1364/OE.22.030063.

[18] F. Ferri, D. Magatti, L. A. Lugiato, and A. Gatti, "Differential ghost imaging," *Phys. Rev. Lett.*, vol. 104, Jun. 2010, Art. no. 253603(4), doi: 10.1103/PhysRevLett.104.253603.

[19] E. Losero, I. Ruo-Berchera, A. Meda, A. Avella, O. Sambataro, and M. Genovese, "Quantum differential ghost microscopy," *Phys. Rev. A*, vol. 100, Dec. 2019, Art. no. 063818(9), doi: 10.1103/PhysRevA.100.063818.

[20] B. Sun, S. S. Welsh, M. P. Edgar, J. H. Shapiro, and M. J. Padgett, "Normalized ghost imaging," *Opt. Exp.*, vol. 20, no. 15, pp. 16892–16901, Jul. 2012, doi: 10.1364/OE.20.016892.

[21] X. Lv *et al.*, "Experimental investigation of iterative pseudoinverse ghost imaging," *IEEE Photon. J.*, vol. 10, no. 3, Jun. 2018, Art. no. 3900708, doi: 10.1109/JPHOT.2018.2832720.

[22] X. R. Yao *et al.*, "Iterative denoising of ghost imaging," *Opt. Exp.*, vol 22, no. 20, pp. 24268–24275, Sep. 2014, doi: 10.1364/OE.22.024268.

[23] A. Smoktunowicz and I. Wróbel, "Numerical aspects of computing the moore-penrose inverse of full column rank matrices," *BIT Numer. Math.*, vol. 52, pp. 503–524, Jun. 2012, doi: 10.1007/s10543-011-0362-0.

[24] V. Katkovnik and J. Astola, "Compressive sensing computational ghost imaging," *J. Opt. Soc. Amer. A*, vol. 29, no. 8, pp. 1556–1567, Aug. 2012, doi: 10.1364/JOSAA.29.001556.

[25] M. Lyu *et al.*, "Deep-learning-based ghost imaging," *Sci. Rep.*, vol. 7, Dec. 2017, Art. no. 17865. [Online]. Available: https://doi.org/10.1038/s41598-017-18171-7

[26] B. J. Hoenders, "Review of a bewildering classical-quantum phenomenon: Ghost imaging," in *Advances in Imaging and Electron Physics*, London, U.K.: Elsever Academic Press, 2018, vol. 208, ch. 1, pp. 1–41, doi: 10.1016/bs.aiep.2018.08.001.

[27] P. A. Moreau, E. Toninelli, T. Gregory, and M. J. Padgett, "Ghost imaging using optical correlations," *Laser Photon. Rev.*, vol. 12, no. 1, Dec. 2017, Art. no. 1700143, doi: 10.1002/lpor.201700143.

[28] J. H. Shapiro and R. W. Boyd, "The physics of ghost imaging," *Quantum Inf. Process.*, vol. 11, pp. 949–993, Jan. 2012. [Online]. Available: https://doi.org/10.1007/s11128-011-0356-5

[29] F. V. Pepe, F. Di Lena, A. Garuccio, G. Scarcelli, and M. D'Angelo, "Correlation plenoptic imaging with entangled photons," *Technologies*, vol. 4, no. 2, p. 17, Jun. 2016, Art. no. 2, doi: 10.3390/technologies4020017.

[30] F. V. Pepe, G. Scarcelli, A. Garuccio, and M. D'Angelo, "Plenoptic imaging with second-order correlations of light," *Quantum Meas. Quantum Metrol.*, vol. 3, no. 1, pp. 20–26, Apr. 2016, doi: 10.1515/qmetro-2016-0004.

[31] S. Hozawa, K. Nitta, and O. Matoba, "Single-shot thermal ghost imaging," in *Proc. Conf. Lasers Electro-Opt. Pacific Rim*, 2013, pp. 1–2, doi: 10.1109/CLEOPR.2013.6600457.

[32] G. Scala, M. D'Angelo, A. Garuccio, S. Pascazio, and F. V. Pepe, "Signal-to-noise properties of correlation plenoptic imaging with chaotic light," *Phys. Rev. A*, vol. 99, May 2019, Art. no. 053808, doi: 10.1103/PhysRevA.99.053808.

[33] M. Gilaberte Basset, F. Setzpfandt, F. Steinlechner, E. Beckert, T. Pertsch, and M. Gräfe, "Perspectives for applications of quantum imaging," *Laser Photon. Rev.*, vol. 13, no. 10, Sep. 2019, Art. no. 1900097(24), doi: 10.1002/lpor.201900097.

[34] R. Penrose, "A generalized inverse for matrices," *Math. Proc. Cambridge Philos. Soc.*, vol. 51, no. 3, pp. 406–413, Jul. 1955, doi: 10.1017/S0305004100030401.

[35] Q. H. Thu and M. Ghanbari, "Scope and validity of PSNR in image/video quality assessment," *Electron. Lett.*, vol. 44, no.13, pp. 800–801, Jun. 2008, doi: 10.1049/el:20080522.

[36] G. Scala, M. D´Angelo, A. Garuccio, S. Pascazio, and F. V. Pepe, "Signal-to-noise properties of correlation plenoptic imaging with chaotic light," *Phys. Rev. A*, vol. 99, May 2019, Art. no. 053808(11), doi: 10.1103/PhysRevA.99.053808.

[37] A. Meda *et al.*, "Photon-number correlation for quantum enhanced imaging and sensing," *J. Opt.*, vol. 19, no. 9, Aug. 2017, Art. no. 094002(27), doi: 10.1088/2040-8986/aa7b27.